Decoupling the Compositional Fluctuation Theory and Polar Nanoregions in Relaxor Ferroelectric Films

Feng-Hui Gong,[1,2,*] Yu-Ting Chen,[1,2,*] Kang-Ming Luo,[3,4,*] Hua-Long Ge,[5] Tao Wang,[6] Yun-Long Tang,[3,4] Jia-Qi Liu,[3,4] Yu-Jia Wang,[3,4] Yin-Lian Zhu,[1,7] and Xiu-Liang Ma[1,2,8,9,†]

[1]*Bay Area Center for Electron Microscopy, Songshan Lake Materials Laboratory, Dongguan, 523808 Guangdong, China*
[2]*Institute of Physics, Chinese Academy of Sciences, Beijing 100190, China*
[3]*Shenyang National Laboratory for Materials Science, Institute of Metal Research, Chinese Academy of Sciences, Shenyang 110016, China*
[4]*School of Materials Science and Engineering, University of Science and Technology of China, Shenyang 110016, China*
[5]*Materials Genome Institute, School of Materials and Energy, Yunnan University, Kunming 650091, China*
[6]*College of Mathematics and Physics, Yibin University, Yibin 644007, China*
[7]*School of Materials Science and Engineering, Hunan University of Science and Technology, Xiangtan 411201, China*
[8]*Quantum Science Center of Guangdong-HongKong-Macau Greater Bay Area, Shenzhen, China*
[9]*State Key Lab of Advanced Processing and Recycling on Non-ferrous Metals, Lanzhou University of Technology, Lanzhou 730050, China*

(Received 2 July 2025; accepted 6 January 2026; published 26 January 2026)

The existence of polar nanoregions (PNRs) endows relaxor ferroelectrics with peculiar behaviors, which is explained using the compositional fluctuation theory (CFT). Here, by designing relaxor ferroelectric films with the same configurational entropy (S_{config}), namely $ATiO_3$ and $PbBO_3$, we show that the compositional heterogeneity is not a prerequisite for PNR formation. Transmission electron microscope experiments show that PNRs exist in both cubic films, and only the $PbBO_3$ film shows remarkable compositional fluctuation, i.e., the formation of PNRs in $ATiO_3$ is not related with the CFT. First-principles calculations indicate that while the mixing enthalpies of element pairs in $ATiO_3$ are generally close to 0, resulting in a nearly homogeneous compositional distribution, those of some element pairs in $PbBO_3$ are large negative values, indicating that the compositional fluctuation is rooted in the large negative mixing enthalpy. This Letter offers a new perspective on the CFT in relaxor ferroelectrics.

DOI: 10.1103/5p94-jpz7

In 1958, $SrTiO_3 - Bi_2O_3 \cdot nTiO_2$ was first found to exhibit relaxation polarization, leading to a high dielectric constant without ferroelectric properties [1]. Two years later, Smolenskii *et al.* discovered that $Pb(Mg_{1/3}Nb_{2/3})O_3$ showed a broad dielectric peak, distinct from conventional ferroelectrics [2], marking the start of relaxor ferroelectrics. Today, by modulating the A- and B-site elements in the perovskite ABO_3 structure, various relaxor ferroelectrics have been synthesized [3–7]. The high-entropy strategy has also been used to enhance energy storage performance by introducing multiple cation species at lattice sites, showing promising applications in advanced power systems [8,9].

Relaxor ferroelectrics are characterized by a gradual phase transition from paraelectric to ferroelectric without a distinct Curie temperature (T_c), known as a diffuse phase transition, which appears as a broad dielectric peak in the temperature-dependent dielectric constant curve [8–11]. The temperature at which the maximum dielectric constant occurs is called the characteristic temperature (T_m). Below T_m, the dielectric constant decreases with increasing frequency, dielectric loss increases, and both peaks shift to higher temperatures [8–11]. The compositional fluctuation theory (CFT) was proposed to explain this behavior [12–16].

Chemical variations across different polar nanoregions (PNRs) arise from the occupation of crystal sites by different elements, leading to compositional fluctuations [12–16]. During cooling, regions sensitive to composition transition first, forming PNRs [12–20]. In the transition range, ferroelectric and paraelectric phases coexist without a distinct transition point [12–20], explaining the diffuse phase transition and frequency dispersion [21–27]. The CFT also supports models like order-disorder theory [28], micro-macro domain transition [29], and random-field models [24,30,31]. Gradually, the origins of random-field formation have expanded to include compositional differences [12–16], defects [30,31], and strain [30,32], enriching the theoretical framework. Recent molecular dynamics simulations also show that PNRs percolate through the film, rather than being embedded in a nonpolar matrix [17].

*These authors contributed equally to this work.
†Contact author: xlma@iphy.ac.cn

However, there has been controversy regarding the CFT and the formation of PNRs. Here, by combining the mixing enthalpy and the valence state fluctuations of elements (Fig. S1), we designed and grew two types of ferroelectric films with the same S_{config} but different enthalpies using pulsed laser deposition (see Methods for details [33]): $(Pb_{0.2}Ba_{0.2}Ca_{0.2}Sr_{0.2}Na_{0.2})TiO_3(ATiO_3)$ and $Pb(Ti_{0.2}Mg_{0.2}Nb_{0.2}Zr_{0.2}Zn_{0.2})O_3(PbBO_3)$. The tolerance factors are 0.90 and 0.88, respectively (see the Appendix for details on the experimental design and growth exploration) [50–60].

X-ray diffraction (XRD) $\theta-2\theta$ scans revealed sharp diffraction peaks for the $ATiO_3$ film [Fig. 1(a)], indexed at (00L), confirming its single-phase nature. The out-of-plane lattice parameter matches that of the $TbScO_3$ (TSO) substrate. High-resolution XRD reciprocal space mappings (RSMs) [Figs. 1(b) and 1(c)] revealed that the film and substrate are coherently aligned, with no deviation in diffraction peaks, indicating the absence of dislocation defects. The average out-of-plane lattice constant of the $ATiO_3$ films is 3.91 Å. Next, selected area electron diffraction (SAED) patterns confirmed that the $ATiO_3$ film has a simple cubic structure [Figs. 1(d)–1(f)]. Traditional space group determination methods using reciprocal space data can lead to ambiguities, especially with glide planes and screw axes. Instead, we used high-angle annular dark-field scanning transmission electron microscopy (HAADF-STEM) imaging to determine space groups in real space. HAADF-STEM images along the [010], [110], and [111] directions allowed us to identify the 2D plane group [Figs. 1(g)–1(i)], revealing symmetry elements of $p4mm$, $p2mm$, and $p6mm$. Both SAED and the 2D plane group confirm that the space group of the $ATiO_3$ film is $Pm\bar{3}m$.

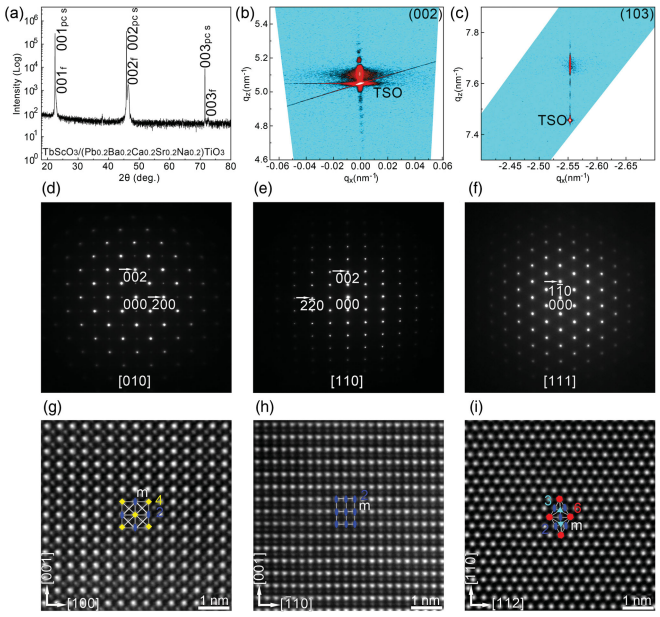

FIG. 1. Space group of $ATiO_3$ films. (a) XRD linear scan of the 30 nm thick $ATiO_3$ films grown on a TSO $(110)_O$ (orthorhombic) substrate. (b), (c) 002 and 103 RSMs of the 30 nm thick $ATiO_3$ films. (d)–(f) SAED patterns of the 360 nm thick $ATiO_3$ films, indexed along the [010], [110], [111] zone axis. (g)–(i) HAADF-STEM images acquired along the [010], [110], [111] directions. The white solid lines represent mirror symmetry planes. Blue ellipses, cyan triangles, yellow quadrilaterals, and red hexagons represent twofold, threefold, fourfold, and sixfold axes, respectively.

The structural analysis of $PbBO_3$ films (Fig. S2) is similar to $ATiO_3$ films. The out-of-plane average lattice constant of $PbBO_3$ is 4.14 Å. Geometric phase analysis confirms a flat, coherent interface between the $PbBO_3$ film and substrate (Fig. S3). Figure S4 shows HAADF-STEM images of $ATiO_3$ and $PbBO_3$ films, with lattice spacing, ion displacement, and rotation angle maps [61]. Despite the films' cubic structure, lattice spacing fluctuations suggest compositional variations affecting lattice expansion or contraction. Additionally, ion displacement analysis shows small displacements, implying low remanent polarization [60,62]. Integrated differential phase contrast images of the $PbBO_3$ film [Fig. S5(a)] revealed variations in oxygen displacement directions across adjacent unit cells, with differential phase contrast images showing local electric field shifts within a few nanometers [Fig. S5(b)]. These observations suggest that both films may exhibit relaxor ferroelectric characteristics.

The direction of spontaneous polarization (P_s) is from the negative charge to the positive charge. In this Letter, the direction of P_s is also opposite to the direction of ion displacement [Figs. S5(c) and S5(d)] [19,20]. Figure 2(a) shows the polarization map from Fig. S4(a), revealing PNRs around a few nanometers, confirming the relaxor ferroelectric properties (see supplementary discussion in the Supplemental Material [33]). X-Ray photoelectron spectroscopy (XPS) measurements show lower binding energy shifts for Pb, Ba, Ca, Sr, and Na, indicating electron gain and valence reduction of A-site atoms due to initial-state and relaxation effects [Figs. 2(b) and 2(c), Fig. S6(a)]. Interestingly, Ti and O peaks also shift to lower binding energy, suggesting a charge imbalance in $ATiO_3$ films. XPS analysis shows Pb^{2+} and Pb^0, Ti^{4+} and Ti^{3+}, the suboxide state of Sr, and oxygen vacancies coexisting to balance charge in the $ATiO_3$ system (Figs. S7 and S8; see supplementary analysis in the Supplemental Material). Figure 2(d) presents the polarization map from Fig. S4(b), revealing PNRs a few nanometers in size, supporting relaxor ferroelectric behavior in $PbBO_3$ films. PNRs are uniformly distributed with smooth polarization transitions at boundaries. The PNRs are not strictly separated, possibly approaching their behavior near the freezing temperature. XPS of $PbBO_3$ films shows shifts in Ti, Mg, Nb, Zr, and Zn peaks to higher binding energies [Figs. 2(e) and 2(f), Fig. S6(b)], suggesting electron loss and increased valence of the B-site atoms. The O peak shifts higher energy [Fig. 2(f)], while Pb shifts lower energy, indicating

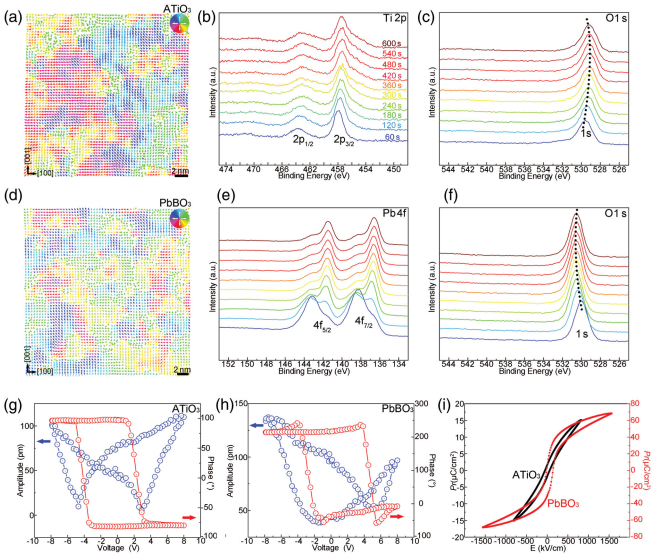

FIG. 2. Relaxation characteristics of ferroelectric $ATiO_3$ and $PbBO_3$ films. (a) The P_s distribution map of the 30 nm thick $ATiO_3$ films. (b), (c) XPS in-depth analyses of Ti $2p$ and O $1s$ spectra for the 360 nm thick $ATiO_3$ films. The etching time is labeled in the image. (d) The P_s distribution map of the 30 nm thick $PbBO_3$ films. (e), (f) XPS in-depth analyses of Pb $4f$ and O $1s$ spectra for the 360 nm thick $PbBO_3$ films. (g), (h) Local piezoresponse force microscopy (PFM) amplitude and phase hysteresis loops for the 30 nm thick films. (i) Out-of-plane P-E loops of the 90 nm thick films.

electron gain and reduced Pb valence [Fig. 2(e)]. These results show oxidation state fluctuations and charge disproportionation. Similarly, the coexistence of Pb^{2+} and Pb^0, Ti^{4+} and Ti^{3+}, Nb^{5+} and Nb^{2+}, and oxygen vacancies helps balance charge in the $PbBO_3$ system (Figs. S9–S11). The butterfly-shaped amplitude loops and square-shaped phase hysteresis along the out-of-plane direction indicate ferroelectric switching [Figs. 2(g) and 2(h)]. The coercive voltage of both films is around 4 V. Both show relaxor ferroelectric behavior, confirmed by PNR analysis, polarization-electric field (P-E) loops [Fig. 2(i)], and dielectric spectroscopy [Fig. S12]. Despite having the same nonpolar $Pm\bar{3}m$ space group, they display similar PNRs and hysteresis loops.

We used super-EDS to probe atomic-scale element distributions in relaxor ferroelectric films. Figures 3(a) and 3(b) show atomic-resolution HAADF-STEM images and super-EDS maps of the $ATiO_3$ films. The Ti element is uniformly distributed, and subtle lattice features of O are captured despite super-EDS's lower sensitivity to light elements. Pb, Ca, and Sr show distinct lattice patterns, while Ba and Na exhibit weak lattice features. The maps reveal a random distribution of A-site elements (Pb, Ba, Ca, Sr, Na) within each atomic column, indicating a disordered A-site lattice. Figure 3(c) highlights this randomness in the 3D structure, and Fig. 3(d) shows line profiles with negligible compositional fluctuations in atomic fractions of each element. We observe peak positions of curve fluctuations, with a valley forming between adjacent peaks due to the spacing of A-site atoms. The Sr shows a stronger signal, and Na a weaker one, but overall, compositional variation is negligible. Figures S13(a)–S13(c) also confirm the A-site disorder. To eliminate the effect of sample thickness (multiple superimposed PNRs), a 5 nm thick freestanding $ATiO_3$ film was fabricated with PNR sizes matching the film thickness (Fig. S14). Super-EDS and line profiles also showed negligible compositional fluctuations in the $ATiO_3$ film (Fig. S15), consistent with the results in Figs. 3(a)–3(d). Figures 3(e) and 3(f) show HAADF-STEM images and super-EDS maps of $PbBO_3$ films. Unlike the $ATiO_3$ film, the five elements (Ti, Mg, Nb, Zr, Zn) in $PbBO_3$ tend to aggregate, with significant inhomogeneous fluctuations and localized clustering in the super-EDS maps [Fig. 3(f)]. Figure 3(g) highlights B-site element clustering in the 3D structure of $PbBO_3$. In the Ti map [Fig. 3(f)], brightness increases with Ti atom density. Nb has the highest atomic fraction, followed by Ti and Zr, while Mg and Zn are lower. The maximum atomic fraction fluctuation reaches 15% [Fig. 3(h)], indicating clustering at adjacent B-site positions in the cubic lattice. Additional experiments also confirm this clustering tendency [Figs. S13(d)–S13(f)].

Finally, density functional theory calculations were performed to quantify the mixing enthalpy contribution to the Gibbs free energy. Three atomic configurations, (111), (110), and (001)-type distributions, were studied to assess the binary mixing enthalpies in $ATiO_3$ and $PbBO_3$ [Fig. 4(a) and Figs. S16 and S17]. The notation (hkl) refers to the stacking sequence of A/B-site cation layers perpendicular to the $(hkl)_{\mathrm{cubic}}$ direction. The results for the (111) configuration, the most experimentally relevant case [63,64], are shown in Figs. 4(b) and 4(c). In $ATiO_3$, binary mixing enthalpies are near 0 kJ/mol, except for Ca-containing pairs with slight negative values. In contrast, $PbBO_3$ shows substantial negative mixing enthalpies for Nb-Mg (−152.84 kJ/mol) and Nb-Zn (−117.92 kJ/mol), while other element pairs fluctuate moderately within approximately ±20 kJ/mol around zero. These characteristics hold across the other configurations (Figs. S16 and S17). Subsequently, the overall mixing enthalpy of $ATiO_3$ and $PbBO_3$ was calculated from the binary mixing enthalpies (see Methods for the calculation of the mixing enthalpy [33]). $ATiO_3$ shows near-zero values [1.098, 1.451, and −2.856 kJ/mol for the (111), (110), and (001) configurations, respectively], indicating that configuration entropy dominates and leads to a nearly ideal disordered solid solution. In contrast, $PbBO_3$ has significantly negative values (−39.584, −35.702, and −46.430 kJ/mol), mainly due to the anomalous Nb-Mg and Nb-Zn pairs, promoting atomic clustering and disrupting the uniform distribution of the disordered solid solution. Importantly, these anomalous enthalpies originate from pairs with unusual valence combinations, Nb(+5)-Mg(+2) and Nb(+5)-Zn(+2),

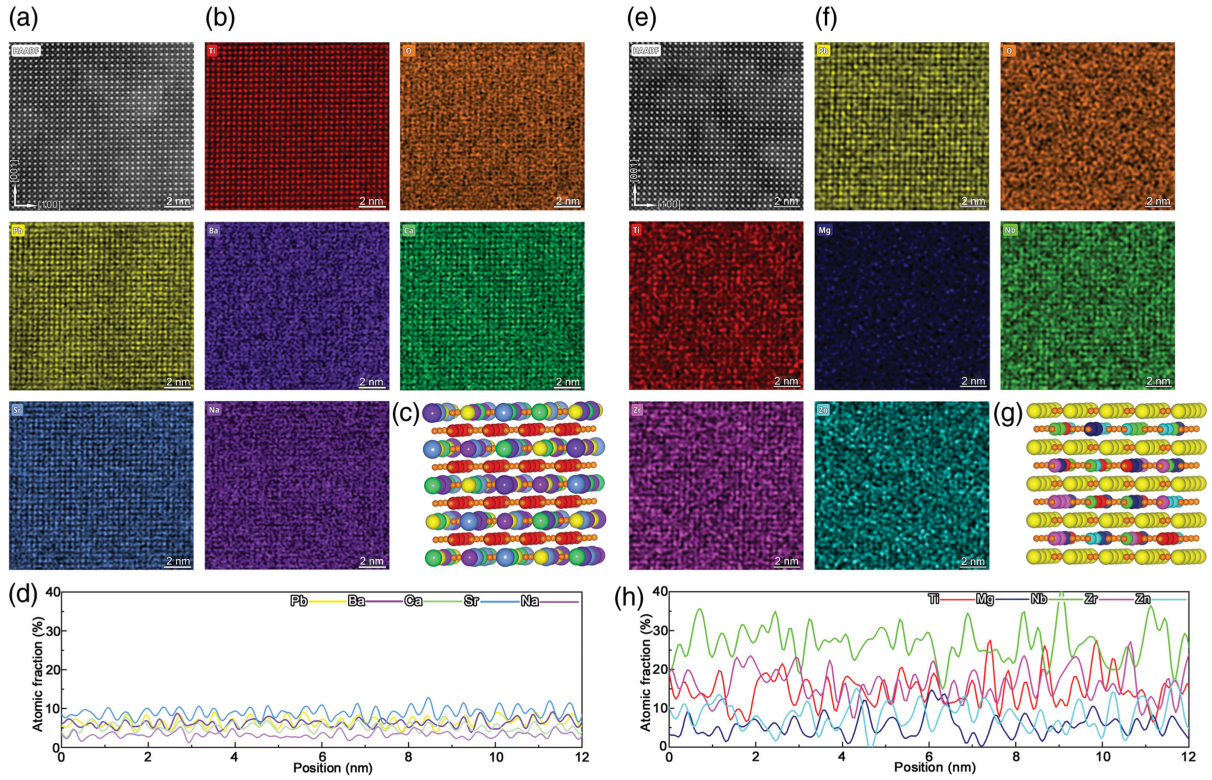

FIG. 3. Compositional fluctuation behavior in relaxor ferroelectric $ATiO_3$ and $PbBO_3$ films. (a),(b) HAADF-STEM images of the 30 nm thick $ATiO_3$ film and corresponding atomic-scale super-EDS maps for Ti, O, Pb, Ba, Ca, Sr, and Na. (c) 3D schematic of the $ATiO_3$ films. (d) Line profiles showing the atomic fraction of individual elements derived from the super-EDS maps in (b). (e), (f) HAADF-STEM images of the 30 nm thick $PbBO_3$ film and corresponding atomic-scale super-EDS maps for Pb, O, Ti, Mg, Nb, Zr, and Zn. (g) 3D schematic of the $PbBO_3$ film. (h) Line profiles showing the atomic fraction of individual elements derived from the super-EDS maps in (f).

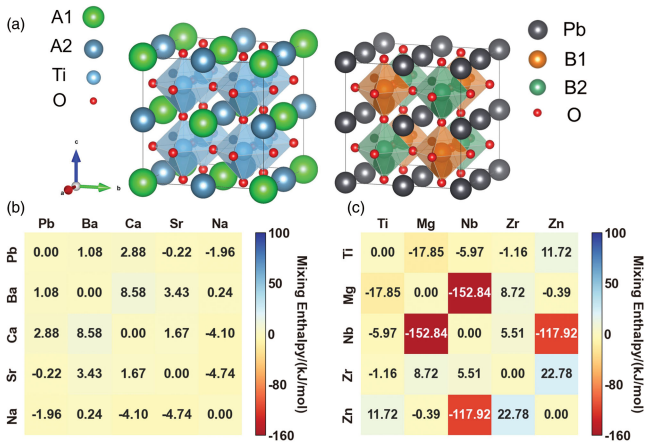

FIG. 4. Atomic configurations and mixing enthalpy of (111)-type binary solid solution. (a) Schematic illustrations of *A*-site (left) and *B*-site (right) configurations. The *A*-site cations (*A*1 and *A*2) are occupied by Pb, Ba, Ca, Sr, and Na, while the *B*-site cations (*B*1 and *B*2) are occupied by Ti, Mg, Nb, Zr, and Zn. (b) Calculated mixing enthalpy for *A*-site binary solid solutions. (c) Calculated mixing enthalpy for *B*-site binary solid solutions.

which corroborates our earlier hypothesis. Unlike studies of artificial architectures with relaxorlike behavior in $BaTiO_3/BaZrO_3$ superlattices [32], this Letter shows that in $ATiO_3$, PNRs can form with minimal enthalpic driving force for chemical clustering, as high configurational entropy alone does not guarantee the presence of chemical fluctuation.

In summary, the STEM experiment reveals the presence of PNRs in both film types, with significant compositional fluctuations in the $PbBO_3$ film, suggesting certain elements cluster. The $ATiO_3$ lacks detectable compositional variations, indicating a more disordered distribution. This indicates that compositional heterogeneity is not a prerequisite for the formation of PNRs. Under the condition of the same S_{config}, first-principles calculations show that while mixing enthalpies in $ATiO_3$ are close to zero, meaning uniform composition, certain element pairs in $PbBO_3$ have large negative mixing enthalpies, causing compositional fluctuations.

Acknowledgments—We are grateful to X. K. Fan and Z. Y. Chen of this laboratory for technical support on the ThermoFisher Spectra 300 aberration-corrected STEM. We thank Chat GPT 4 for helping us with the grammar check

and language refinement of this work. We are grateful to Professors Q. Yu, S. Liu, and B. B. Yang for their valuable discussions. This work is supported by the National Natural Science Foundation of China (No. 52471022, No. 52122101, No. U24A2013, No. 12504020, and No. 12504116), the National Key Research and Development Program of China (No. 2024YFA1408000), Guangdong Provincial Quantum Science Strategic Initiative (No. GDZX2202001 and No. GDZX2302001), and the IMR Innovation Fund (No. 2024-ZD01). F.-H. G. acknowledges the China National Postdoctoral Program for Innovative Talents (No. BX20240245) and the China Postdoctoral Science Foundation (No. 2024M752303) for their support. Y.-T. C. acknowledges the China Postdoctoral Science Foundation (No. 2023M742519) for their support. Y.-J. W. acknowledges the Youth Innovation Promotion Association CAS (No. 2021187).

Data availability—The data that support the findings of this article are openly available [65]; embargo periods may apply.

[1] G. I. Skanavi, IA. M. Ksendzov, V. A. Trigubenko, and V. G. Prokhvatilov, Relaxation polarization and losses in nonferroelectric dielectrics with high dielectrics constants, Sov. Phys. JETP **6**, 250 (1958).

[2] G. A. Smolenskii and A. I. Agranovskaya, Dielectric polarization of a number of complex compounds, Sov. Phys. Solid State **1**, 1429 (1960).

[3] L. E. Cross, Relaxor ferroelectrics: An overview, Ferroelectrics **151**, 305 (1994).

[4] N. J. Donnelly, G. Catalan, C. Morros, R. M. Bowman, and J. M. Gregg, Dielectric and electromechanical properties of $Pb(Mg_{1/3}, Nb_{2/3})O_3 - PbTiO_3$ thin films grown by pulsed laser deposition, J. Appl. Phys. **93**, 9924 (2003).

[5] C. R. Qiu *et al.*, Transparent ferroelectric crystals with ultrahigh piezoelectricity, Nature (London) **577**, 350 (2020).

[6] Y. Y. Zhang, L. Chen, H. Liu, S. Q. Deng, H. Qi, and J. Chen, High-performance ferroelectric based materials via high-entropy strategy: Design, properties, and mechanism, InfoMat **5**, e12488 (2023).

[7] C. Liu *et al.*, Advances in high entropy oxides: Synthesis, structure, properties and beyond, Prog. Mater. Sci. **148**, 101385 (2025).

[8] H. Pan *et al.*, Ultrahigh energy storage in superparaelectric relaxor ferroelectrics, Science **374**, 100 (2021).

[9] B. B. Yang *et al.*, Engineering relaxors by entropy for high energy storage performance, Nat. Energy **8**, 956 (2023).

[10] L. Shu *et al.*, Partitioning polar-slush strategy in relaxors leads to large energy-storage capability, Science **385**, 204 (2024).

[11] H. Zheng *et al.*, Heterogeneous field response of hierarchical polar laminates in relaxor ferroelectrics, Science **384**, 1447 (2024).

[12] G. A. Smolensky and V. A. Isupov, Thermodynamics of ferroelectrics with the structure of the K-W-bronze, Ferroelectrics **8**, 443 (1974).

[13] G. A. Smolensky, V. A. Isupov, B. Baitamayev, and A. F. Ioffe, Outlook at the further development of the perovskite piezoelectric ceramic, Ferroelectrics **44**, 167 (1982).

[14] G. A. Smolensky, V. A. Bokov, V. A. Isupov, N. N. Krainik, R. E. Pasynkov, A. I. Sokolov, and N. K. Yushin, *The Physics of Ferroelectric Properties* (Nauka, Leningrad, 1985) (in Russian).

[15] S. B. Vakhrushev, V. A. Isupov, B. E. Kvyatkovsky, N. M. Okuneva, I. P. Pronin, G. A. Smolensky, and P. P. Syrnikov, Phase transitions and soft modes in sodium bismuth titanate, Ferroelectrics **63**, 153 (1985).

[16] A. A. Bokov and V. Y. Shonov, Dielectric properties and diffusion of ferroelectric phase transition in lead indium niobate, Ferroelectrics **108**, 237 (1990).

[17] H. Takenaka, I. Grinberg, S. Liu, and A. M. Rappe, Slush-like polar structures in single-crystal relaxors, Nature (London) **546**, 391 (2017).

[18] M. J. Krogstad *et al.*, The relation of local order to material properties in relaxor ferroelectrics, Nat. Mater. **17**, 718 (2018).

[19] J. Kim *et al.*, Size-driven phase evolution in ultrathin relaxor films, Nat. Nanotechnol. **20**, 478 (2025).

[20] A. Kumar, J. N. Baker, P. C. Bowes, M. J. Cabral, S. J. Zhang, E. C. Dickey, D. L. Irving, and J. M. LeBeau, Atomic-resolution electron microscopy of nanoscale local structure in lead-based relaxor ferroelectrics, Nat. Mater. **20**, 62 (2021).

[21] S. N. Gvasaliya, S. G. Lushnikov, and B. Roessli, Disorder and relaxation mode in the lattice dynamics of the $PbMg_{1/3}Nb_{2/3}O_3$ relaxor ferroelectric, Phys. Rev. B **69**, 092105 (2004).

[22] H. H. Su, C. S. Hong, C. C. Tsai, and S. Y. Chu, Dielectric behaviors of $Ba(Mg_{1/3}Nb_{2/3})O_3$ modified $(Na_{0.5}K_{0.5})NbO_3$ ceramics, Ceram. Int. **44**, 7955 (2018).

[23] M. Venet, J. C. M'Peko, F. L. Zabotto, F. Guerrero, D. Garcia, and J. A. Eiras, Dynamics of normal to diffuse and relaxor phase transition in lead metaniobate-based ferroelectric ceramics, Appl. Phys. Lett. **94**, 172901 (2009).

[24] V. Westphal, W. Kleemann, and M. D. Glinchuk, Diffuse phase transitions and random-field-induced domain states of the "relaxor" ferroelectric $PbMg_{1/3}Nb_{2/3}O_3$, Phys. Rev. Lett. **68**, 847 (1992).

[25] M. Venet, J. de Los S. Guerra, I. A. Santos, J. A. Eiras, and D. Garcia, Diffuse phase transition and relaxor behaviour of textured $Sr_{0.63}Ba_{0.37}Nb_2O_6$ ceramics, J. Phys. Condens. Matter **19**, 026207 (2007).

[26] J. Wang, Z. H. Zhou, and J. M. Xue, Phase transition, ferroelectric behaviors and domain structures of $(Na_{1/2}Bi_{1/2})_{1-x}TiPb_xO_3$ thin films, Acta Mater. **54**, 1691 (2006).

[27] X. Xia, C. B. Li, J. T. Zeng, L. Y. Zheng, and G. R. Li, Scaling behavior of dynamic hysteresis of PMN-PT relaxor ferroelectric ceramics near the morphotropic phase boundary, J. Am. Ceram. Soc. **103**, 2694 (2020).

[28] N. Dragoe and D. Berardan, Order emerging from disorder, Science **366**, 573 (2019).

[29] Z. L. Chen, X. Yao, and L. E. Cross, Depolarization behavior, and reversible pyroelectricity in lead scandium-tantalate ceramics under DC biases, Ferroelectrics **49**, 213 (1983).

[30] W. Kleemann, Random-field induced antiferromagnetic ferroelectric and structural domain states, Int. J. Mod. Phys. B **07**, 2469 (1993).

[31] R. Pirc and R. Blinc, Spherical random-bond-random-field model of relaxor ferroelectrics, Phys. Rev. B **60**, 13470 (1999).

[32] Z. S. Tian, M. Xu, J. Kim, H. Pan, D. Lou, X. Huang, J. M. LeBeau, and L. W. Martin, Tunable artificial relaxor behavior in $[BaTiO_3]_m/[BaZrO_3]_n$ superlattices, Phys. Rev. Lett. **130**, 266801 (2023).

[33] See Supplemental Material at http://link.aps.org/supplemental/10.1103/5p94-jpz7 for more details on experimental and simulation methods, which includes Refs. [34–41] and for a discussion of Why PNRs fail to manifest in chemically "pure" materials, which includes Refs. [42–49].

[34] G. Kresse and D. Joubert, From ultrasoft pseudopotentials to the projector augmented-wave method, Phys. Rev. B **59**, 1758 (1999).

[35] J. P. Perdew, A. Ruzsinszky, G. I. Csonka, O. A. Vydrov, G. E. Scuseria, L. A. Constantin, X. L. Zhou, and K. Burke, Restoring the density-gradient expansion for exchange in solids and surfaces, Phys. Rev. Lett. **100**, 136406 (2008).

[36] K. Momma and F. Izumi, VESTA 3 for three-dimensional visualization of crystal, volumetric and morphology data, J. Appl. Crystallogr. **44**, 1272 (2011).

[37] Z. B. An *et al.*, Negative mixing enthalpy solid solutions deliver high strength and ductility, Nature (London) **625**, 697 (2024).

[38] Y. Zhang, Y. J. Zhou, J. P. Lin, G. L. Chen, and P. K. Liaw, Solid-solution phase formation rules for multi-component alloys, Adv. Eng. Mater. **10**, 534 (2008).

[39] S. Guo and C. T. Liu, Phase stability in high entropy alloys: Formation of solid solution phase or amorphous phase, Prog. Nat. Sci. Mater. **21**, 433 (2011).

[40] J. E. Morral and S. A. Chen, A regular solution model for a single-phase high entropy and enthalpy alloy, J. Phase Equilib. Diffus. **38**, 382 (2017).

[41] B. P. Burton, Why $Pb(B_{1/3}B'_{2/3})O_3$ perovskites disorder more easily than $Ba(B_{1/3}B'_{2/3})O_3$ perovskites and the thermodynamics of 1:1-type short-range order in PMN, J. Phys. Chem. Solids **61**, 327 (1999).

[42] I. W. Chen and Y. Wang, A domain wall model for relaxor ferroelectrics, Ferroelectrics **206**, 245 (1998).

[43] L. Kaufman and M. Cohen, Thermodynamics and kinetics of martensitic transformations, Prog. Metal Phys. **7**, 165 (1958).

[44] S. Pöykkö and D. J. Chadi, *Ab initio* study of 180° domain wall energy and structure in $PbTiO_3$, Appl. Phys. Lett. **75**, 2830 (1999).

[45] R. K Behera, C. W. Lee, D. Lee, A. N. Morozovska, S. B. Sinnott, A. Asthagiri, V. Gopalan, and S. R Phillpot, Structure, and energetics of 180° domain walls in $PbTiO_3$ by density functional theory, J. Phys. Condens. Matter **23**, 175902 (2011).

[46] Y. J. Wang *et al.*, Polar meron lattice in strained oxide ferroelectrics, Nat. Mater. **19**, 881 (2020).

[47] S. Das *et al.*, Observation of room-temperature polar skyrmions, Nature (London) **568**, 368 (2019).

[48] W. P. Gao *et al.*, Real-space charge-density imaging with sub-ångström resolution by four-dimensional electron microscopy, Nature (London) **575**, 480 (2019).

[49] D. Lee *et al.*, Emergence of room-temperature ferroelectricity at reduced dimensions, Science **349**, 1314 (2015).

[50] C. M. Rost, E. Sachet, T. Borman, A. Moballegh, E. C. Dickey, D. Hou, J. L. Jones, S. Curtarolo, and J. P. Maria, Entropy-stabilized oxides, Nat. Commun. **6**, 8485 (2015).

[51] S. J. McCormack and A. Navrotsky, Thermodynamics of high entropy oxides, Acta Mater. **202**, 1 (2021).

[52] L. Su, H. X. Huyan, A. Sarkar, W. P. Gao, X. X. Yan, C. Addiego, R. Kruk, H. Hahn, and X. Q. Pan, Direct observation of elemental fluctuation and oxygen octahedral distortion-dependent charge distribution in high entropy oxides, Nat. Commun. **13**, 2358 (2022).

[53] Y. J. Wang *et al.*, High entropy nonlinear dielectrics with superior thermally stable performance, Adv. Mater. **35**, 2304128 (2023).

[54] B. L. Musico, D. Gilbert, T. Z. Ward, K. Page, E. George, J. Q. Yan, D. Mandrus, and V. Keppens, The emergent field of high entropy oxides: Design, prospects, challenges, and opportunities for tailoring material properties, APL Mater. **8**, 040912 (2020).

[55] L. Chen, H. F. Yu, J. Wu, S. Q. Deng, H. Liu, L. F. Zhu, H. Qi, and J. Chen, Large energy capacitive high-entropy lead-free ferroelectrics, Nano Micro Lett. **15**, 65 (2023).

[56] Y. G. Pu *et al.*, (Mg,Mn,Fe,Co,Ni)O: A rocksalt high-entropy oxide containing divalent Mn and Fe, Sci. Adv. **9**, eadi8809 (2023).

[57] L. Y. Yang *et al.*, Simultaneously achieving giant piezoelectricity and record coercive field enhancement in relaxor-based ferroelectric crystals, Nat. Commun. **13**, 2444 (2022).

[58] Y. Y. Huang, K. L. Shang, Y. L. Yang, W. J. Shi, L. Y. Zhang, V. Laletin, V. Shur, R. Y. Jing, and L. Jin, Ultrahigh energy storage capacities in high-entropy relaxor ferroelectrics, J. Mater. Chem. A. **12**, 18224 (2024).

[59] X. Y. Feng, Z. Y. An, N. Zhang, S. Yang, M. W. Wang, C. Wang, Y. Li, X. C. Liu, and F. Li, Lattice parameter fluctuations of relaxor ferroelectrics determined by X-ray diffraction method, J. Am. Ceram. Soc. **106**, 2580 (2023).

[60] F. H. Gong, Y. L. Tang, Y. J. Wang, Y. T. Chen, B. Wu, L. X. Yang, Y. L. Zhu, and X. L. Ma, Absence of critical thickness for polar skyrmions with breaking the Kittel's law, Nat. Commun. **14**, 3376 (2023).

[61] S. C. Abrahams, S. K. Kurtz, and P. B. Jamieson, Atomic displacement relationship to Curie temperature and spontaneous polarization in displacive ferroelectrics, Phys. Rev. **172**, 551 (1968).

[62] T. Wang *et al.*, Large enhancement of ferroelectric properties of perovskite oxides via nitrogen incorporation, Sci. Adv. **11**, eads8830 (2025).

[63] H. C. Wang and W. A. Schulze, Order-disorder phenomenon in lead scandium tantalate, J. Am. Ceram. Soc. **73**, 1228 (1990).

[64] J. Chen, H. M. Chan, and M. P. Harmer, Ordering structure and dielectric properties of undoped and La/Na-doped $Pb(Mg_{1/3}Nb_{2/3})O_3$, J. Am. Ceram. Soc. **72**, 593 (1989).

[65] Available online at https://zenodo.org/records/18171612.

End Matter

Appendix: Experimental design and growth exploration—Taking the ABO_3 perovskite structure as the base unit, we selected five elements with equal molar ratios for both the *A*-site and *B*-site positions, respectively. Thin films are classified as high-, medium-, or traditional-entropy when the S_{config} is greater than 1.5R, between 1R and 1.5R, or less than 1R, respectively. Based on the equation [50–52]

$$S_{\text{config}} = -R\left[\left(\sum_{i=1}^{N} x_i \ln x_i\right)_{\text{cation-site}} + \left(\sum_{j=1}^{M} x_j \ln x_j\right)_{\text{anion-site}}\right], \tag{A1}$$

with R, N (M), and $x_i(x_j)$ representing the ideal gas constant, atomic species and contents at the cation (anion) sites, respectively, we calculated the S_{config} of the $ATiO_3$ and $PbBO_3$ to be 1.6R, which satisfies the compositional design requirements for the same high-entropy values. We also noticed that the valence fluctuations of *A*-site elements are relatively small, while the valence fluctuations of *B*-site elements are more pronounced, as shown in Fig. S1. Moreover, we computed their tolerance factors (t) using the following equation [50,53]:

$$t = \frac{r_A + r_O}{\sqrt{2}(r_B + r_O)}, \tag{A2}$$

where r_A, r_B, and r_O are the ionic radii of the *A*-site, *B*-site, and oxygen element, respectively. Previously synthesized high-entropy oxides are more likely to form high symmetry structures [54–60]. The t is used to determine the structural stability. The reference range for t is 0.77–1.11, with films exhibiting t values between 0.90 and 1.11 being more likely to form a cubic structure. The t values of the $ATiO_3$ and $PbBO_3$ are 0.90 and 0.88, respectively. These values suggest that both $ATiO_3$ and $PbBO_3$ films tend to form solid solutions with a preference for the cubic structure. The lattice constant becomes difficult to predict when multiple elements are mixed to form a solid solution. By exploring film growth on different substrates, the optimal substrate is selected by matching the film's lattice constant, crystal structure, and overall quality. This helps rule out the possibility that PNRs are caused by random fields induced by defects or misfit strain.